# Electro-optically modulated polarizing Fourier-transform spectrometer for plasma spectroscopy applications

John Howard

A new electro-optically modulated optical solid-state (MOSS) interferometer has been constructed for measurement of quantities related to the low-order spectral moments of line emission from optically thin radiant media such as plasmas. When Doppler broadening is dominant, the spectral moments give the Radon transform of corresponding moments of the velocity distribution function of the radiating species. The instrument, which is based on the principle of the Fourier-transform spectrometer, has high etendue and is rugged and compact. When electro-optical path-length modulation techniques are employed, the spectral information is encoded in the temporal frequency domain at harmonics of the modulation frequency and can be obtained by use of a single photodetector. Specifically, for a plasma in drifting local thermodynamic equilibrium the zeroth moment (brightness) is given by the average signal level, the first moment (shift) by the interferometric phase, and the second moment (linewidth) by the fringe visibility. To illustrate the MOSS performance, I present spectroscopic measurements of the time evolution of the plasma ion temperature and flow velocity for rf-heated discharges in the H-1 heliac, a toroidal plasma magnetic confinement at the Australian National University. 

*OCIS codes:* 300.6550, 300.6300, 300.2140, 280.2490, 110.6960.

## 1. Introduction

In this paper I describe an electro-optically modulated optical solid-state (MOSS) spectrometer for general-purpose optical plasma spectroscopy.[1] The spectrometer monitors the temporal coherence of an isolated spectral line by polarization interferometric techniques. It is essentially a Fourier-transform spectrometer (FTS) modulated about a fixed delay. The visibility of the interference fringes produced by the modulation is related to the light temporal coherence whereas the phase conveys variations in the line-center frequency. In its simplest form, the instrument is suited to applications in which the spectral line shape can be characterized by no more that a few free parameters, and in this paper I consider mainly the case in which Doppler broadening of the natural line shape is dominant. Extensions of the instrument to allow observation simultaneously at a multiplicity of fixed delays as well as applications in polarization spectroscopy are discussed elsewhere.[2]

Doppler spectroscopy is a powerful technique for the sensing of the gross features of the velocity distribution function of excited species in radiating, optically thin media such as plasmas, flames, and auroras. Despite the simple linear mapping from the velocity distribution function to the emission spectrum, interpretation is complicated by the fact that the Doppler shift conveys only the velocity component in the direction of view. For extended inhomogeneous media, the spectral line shape is the result of intensity-weighted contributions from all positions along the line of sight. Even when measurements can be made along many viewing lines, the general inverse problem remains ill-posed. However, an important special case for which an inverse exists is the drifting isotropic velocity distribution function. More particularly, when the distribution is in local thermal equilibrium, it can be characterized by three spatially varying parameters, namely, the emission brightness, the first-moment drift velocity, and the species temperature. The Radon (line-integral) transform of the brightness-weighted bulk drift and the temperature of the ion or atom velocity distribution function can be obtained from the low-order spectral moments of the line-integrated emis-

The author is with the Plasma Research Laboratory, Australian National University, Canberra, Australian Capital Territory 0200, Australia. His e-mail address is john.howard@anu.edu.au.

Received 30 January 2001; revised manuscript received 20 August 2001.

0003-6935/02/010197-12$15.00/0

sion. Because of this simple relationship, we find it desirable to record the three lowest-order moments directly by exploiting the spectral response of the dispersing instrument.

For this purpose, my colleagues and I developed a modulated solid-state polarization interferometer based on the principle of the FTS. When the line-center frequency changes (because of Doppler drift), the interferogram phase varies (much like an accordion), leaving the envelope unchanged. On the other hand, when the line shape (e.g., Doppler width) changes, only the fringe visibility is affected, the carrier phase remaining undisturbed. As shown in this paper, this decoupling of first- and higher-order spectral moments is one of the more important fundamental advantages offered by time-domain spectroscopic methods applied to spectroscopy of extended radiating sources. In Section 2 I obtain an expression for the complex coherence of Doppler-broadened line emission from an inhomogeneous radiating source in terms of line integrals of simple scalar and vector fields characterizing the source velocity distribution function.

In Section 3 I describe the optical construction and features of the MOSS spectrometer. Based on an electro-optic birefringent crystal, the instrument is compact and robust and has high optical throughput (compared with a grating spectrometer of comparable resolving power). Because the line-integrated spectral information is carried in the temporal frequency domain at low harmonics of the modulation frequency, it can be adapted easily for truly two-dimensional, time-resolved spectroscopic imaging applications. The details of the instrument function are considered in Section 4.

In Section 5 I show the test results obtained with optical sources of known spectral properties. In one case I confirm the expected variation of fringe contrast with magnetic field strength for a simple Zeeman triplet. The orthogonality and linearity of extracted quantities are also confirmed by a phase-modulated laser source. Finally, in Section 6 I present measurements of the line-integrated brightness, flow, and temperature fields in the H-1 heliac,[3] a helical-axis toroidal magnetic confinement device at the H-1NF National Plasma Fusion Research Facility at the Australian National University.

## 2. Doppler Spectroscopy

For extended, inhomogeneous media such as plasmas, and under conditions in which the line emission (center frequency $\nu_0$) is optically thin and the line shape is determined predominantly by the Doppler effect, a measured emission line spectrum is the sum of contributions having spatially varying intensities, widths (temperatures), and shifts (drifts) along the line of sight. One of the problems attending grating-based Doppler spectroscopy is the difficulty in interpretation of the resulting complex spectrum. Under Fourier transformation, however, the drift and temperature contributions to the spectrum separate, being encoded, respectively, by the phase and amplitude of the corresponding interferogram. In this section I quantify this result and indicate how established inversion methods can be used to obtain the spatial variation of the unknown velocity distribution parameters. Apart from other instrumental advantages, this result is one of the primary motivations for the development of the MOSS spectrometer.

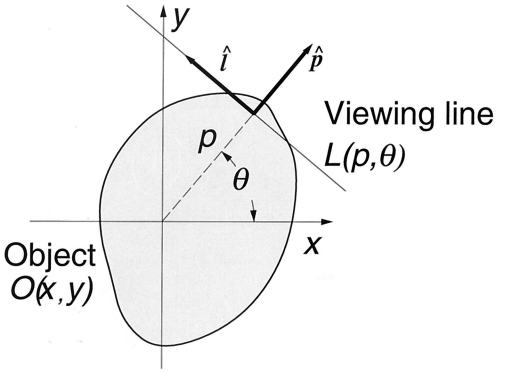


Fig. 1. Geometry for tomography of some two-dimensional scalar function $O$ showing the relationship between unit vector $\hat{\mathbf{l}}$ and the viewing line $L(p, \theta)$ at impact parameter $p$ and angle $\theta$.

We consider an inhomogeneous drifting isotropic velocity distribution function $f(\mathbf{r}, \boldsymbol{\upsilon} - \boldsymbol{\upsilon}_D) \equiv f_0(\mathbf{r}, \upsilon)$ where $\boldsymbol{\upsilon} = \mathbf{V}/c$ is a normalized velocity coordinate, $\upsilon = |\boldsymbol{\upsilon}|$, and $\boldsymbol{\upsilon}_D(\mathbf{r})$ is the local first-moment drift velocity. The integrated measurement along some line $L$ viewing the plasma in direction $\hat{\mathbf{l}}$ (see Fig. 1) is proportional to

$$e(\xi; \hat{\mathbf{l}}) = \int_L g(\mathbf{r}, \xi; \hat{\mathbf{l}}) \mathrm{d}l, \tag{1}$$

where $\xi = (\nu - \nu_0)/\nu_0$ is a normalized optical frequency coordinate and

$$g(\mathbf{r}, \xi; \hat{\mathbf{l}}) = \int f(\mathbf{r}, \boldsymbol{\upsilon} - \boldsymbol{\upsilon}_D) \delta(\xi - \boldsymbol{\upsilon} \cdot \hat{\mathbf{l}}) \mathrm{d}\boldsymbol{\upsilon} \tag{2}$$

is the local emission spectrum. The delta function selects the part of the velocity distribution $f$ that contributes through the Doppler effect to the optical intensity at normalized frequency $\xi$. The Fourier transform of Eq. (2) separates the contributions from the drift and the body of the distribution:

$$G(\mathbf{r}, \phi\hat{\mathbf{l}}) \equiv \mathcal{F}[g(\mathbf{r}, \xi; \hat{\mathbf{l}})] = \exp(i\phi\boldsymbol{\upsilon}_D \cdot \hat{\mathbf{l}}) G_0(\mathbf{r}, \phi). \tag{3}$$

$G_0(\mathbf{r}, \phi)$ is a central slice of the Fourier transform of the spherically symmetric distribution $f_0(\mathbf{r}, \upsilon)$.

We can obtain the Fourier transform optically using interferometric techniques. For an isolated spectral line, the ideal FTS signal intensity can be expressed as

$$S_{\pm}(\phi) = \frac{\mu_0}{2} \{1 \pm \mathcal{R}[\gamma(\phi; \hat{\mathbf{l}}) \exp(i\phi)]\}, \tag{4}$$

where $\phi = 2\pi\nu_0\tau$ in which $\tau$ is the interferometer time delay and $\gamma(\phi; \hat{\mathbf{l}})$ is the optical coherence, related to

the light spectral distribution through the Weiner–Khinchine theorem:

$$\gamma(\phi;\,\hat{\mathbf{l}}) = \frac{1}{\mu_0}\int_{-\infty}^{\infty} e(\xi;\,\hat{\mathbf{l}})\exp(i\phi\xi)\mathrm{d}\xi. \tag{5}$$

The quantity $\mu_0$ is the line integral of the spectrally integrated isotropic emission intensity $I_0(\mathbf{r})$:

$$I_0(\mathbf{r}) \equiv G_0(\mathbf{r},\,0) = \int g(\mathbf{r},\,\xi;\,\hat{\mathbf{l}})\mathrm{d}\xi. \tag{6}$$

By modulating the phase delay $\phi$, we can simultaneously measure both the dc light intensity ($\mu_0$) and the complex coherence, whose modulus (the fringe visibility) is obtained when we combine Eqs. (1)–(3) and Eq. (5):

$$|\gamma(\phi;\,\hat{\mathbf{l}})| = \frac{1}{\mu_0}\int_L G_0(\mathbf{r},\,\phi)\mathrm{d}l. \tag{7}$$

As a result of the Fourier transform of Eq. (3), the fringe visibility is independent of the spatially varying drift $\mathbf{v}_D$ and can be inverted for the isotropic but inhomogeneous distribution function $f_0(\mathbf{r}, \upsilon)$. Under conditions of local thermodynamic equilibrium, the local coherence assumes a particularly simple form:

$$\begin{aligned} G_0(\mathbf{r},\,\phi) &= I_0(\mathbf{r})\exp(-\phi^2\upsilon_{\mathrm{th}}^2/4) \\ &= I_0(\mathbf{r})\exp[-T_S(\mathbf{r})/T_C], \end{aligned} \tag{8}$$

where $T_S(\mathbf{r})$ is the local species temperature. The characteristic temperature $T_C$ is given by

$$kT_C = \frac{1}{2}\,m_S\upsilon_C^2, \tag{9}$$

with characteristic velocity set by the total interferometer phase delay $\phi$:

$$\upsilon_C = \frac{2c}{\phi}. \tag{10}$$

The fringe visibility can now be written as

$$|\gamma(\phi;\,\hat{\mathbf{l}})| = \frac{1}{\mu_0}\int_L I_0(\mathbf{r})\exp[-T_S(\mathbf{r})/T_C]\mathrm{d}l, \tag{11}$$

and tomographic inversion yields $T_S(\mathbf{r})$ (the intensity $I_0$ being obtained from $\mu_0$). As I show below, the visibility is most sensitive to source temperature changes when the characteristic temperature (delay) is chosen so that $T_S \approx T_C$.

The change in the interferometer phase that is due to the Doppler shift is given (to first order in small quantities) by

$$\frac{\delta\phi}{\phi} = \frac{1}{\mu_0|\gamma|}\int_L G_0(\mathbf{r},\,\phi)\mathbf{v}_D \cdot \mathrm{d}\mathbf{l}, \tag{12}$$

where $\mathrm{d}\mathbf{l} \equiv \hat{\mathbf{l}}\mathrm{d}l$. Observe that the usually small Doppler-shift component is magnified by the approximately constant fixed phase delay offset $\phi$. Equation (12) is a vector field line integral whose inversion gives the vorticity of the field $G_0\mathbf{v}_D$. Under certain conditions, it is possible to reconstruct the component of the flow-field vector potential that is normal to the measurement plane.[4]

## 3. Modulated Optical Solid-State Spectrometer

### A. Measurement Principle

It is apparent from Eqs. (4), (11), and (12) that measurements of the interferogram at quadrature phase offsets are sufficient to yield line-integral measurements of the scalar fields $I_0$ (intensity) and $G_0$ (spectral width) and longitudinal line-integral measurements of the vector field $G_0\mathbf{v}_D$ (spectral shift). The simplest approach to obtain these measurements is to sinusoidally modulate the phase delay $\phi$ by $\phi_1 \gtrsim \pi/2$ about some offset delay $\phi_0$ that is chosen to maximize sensitivity to variations in either $T_S$ or $\mathbf{v}_D$. For the instantaneous phase shift, we write

$$\phi = \phi_0 + \phi_1 \sin \Omega t \tag{13}$$

so that the available information bandwidth is determined by the modulation angular frequency $\Omega$. Substituting for $\phi$ in Eq. (4) and applying simple trigonometric identities, we obtain

$$\begin{aligned} S_{\pm}(\phi) = \mu_0[1 &\pm \tilde{\gamma}_c \cos(\phi_1 \sin \Omega t) \\ &\mp \tilde{\gamma}_q \sin(\phi_1 \sin \Omega t)], \end{aligned} \tag{14}$$

where $\tilde{\gamma} = \tilde{\gamma}_c + i\tilde{\gamma}_q = |\gamma| \exp(i\phi_0 + i\delta\phi)$. From the Bessel expansion (see Appendix A), the even and odd harmonics of the modulation frequency are proportional, respectively, to $\tilde{\gamma}_c$ and $\tilde{\gamma}_q$. The approach is optimum in that the three independent pieces of information carried at dc and odd and even harmonics of $\Omega$, namely, $\mu_0$, $\gamma_c$, and $\gamma_q$, relate directly to the unknown velocity distribution parameters $I_0$, $T_S$, and $\mathbf{v}_D$.

Figure 2 illustrates the measurement concept. The path length is modulated about an initial path offset (or operating point) that is sufficiently large to accentuate small changes in line-center frequency. These changes are conveyed by the change in the ratio of even and odd harmonics generated by the modulation. The measured fringe visibility allows an estimate of the species temperature. Solid piezoscanned Michelson interferometers based on this concept have been used for study of the wind and temperature fields of the aurora and planetary atmospheres.[5–7]

### B. Instrument Overview

The principal difficulty with the standard optical FTS is its sensitivity to mechanical and acoustic noise. To overcome this, my colleagues and I constructed an interferometer based on solid polarizing components as illustrated in Fig. 3. To obtain the desired phase delay and modulation, we use optical crystals such as

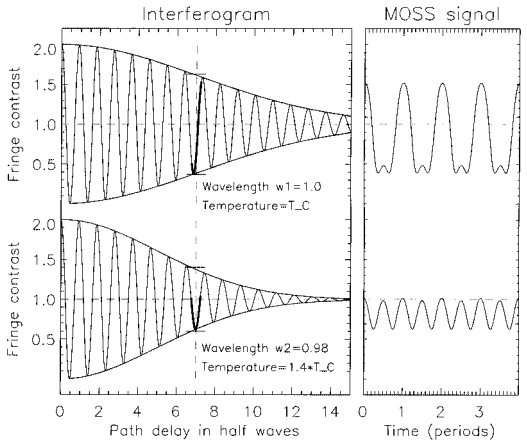


Fig. 2. Simulated interferograms showing the effect on the interferogram phase of a change in line-center frequency (exaggerated for clarity). The dashed vertical line corresponds to the delay introduced by the birefringent crystal, and the bold section is the portion of the interferogram swept by the electro-optic modulation. The fringe contrast also varies with changes in the temperature of the emitting species.

lithium niobate ($LiNbO_3$) that are both birefringent and electro-optic.

Collimated light that was coupled to the system either directly or by lens-coupled optical fibers passes through a suitable prefilter (for example, an optical interference filter) that isolates the spectral line of interest. The filtered beam traverses the first polarizing cube that transmits the horizontally polarized component. Light from the reject port can be relayed to additional instruments (Fig. 3). With the alternative polarizer input port it is also possible to introduce, for example, a calibration light source.

The polarized radiation next traverses a birefringent $LiNbO_3$ plate having its optic axis (or $Z$ axis) oriented at 45° to the plane of polarization. $LiNbO_3$ is a man-made birefringent crystal that exhibits pyroelectric, piezoelectric, photoelastic, ferroelectric, and electro-optic effects.[8] The interferometer makes use of the birefringence ($n_E = 2.25$, $n_O = 2.35$, $B = n_E - n_O \approx -0.1$) and the linear electro-optic

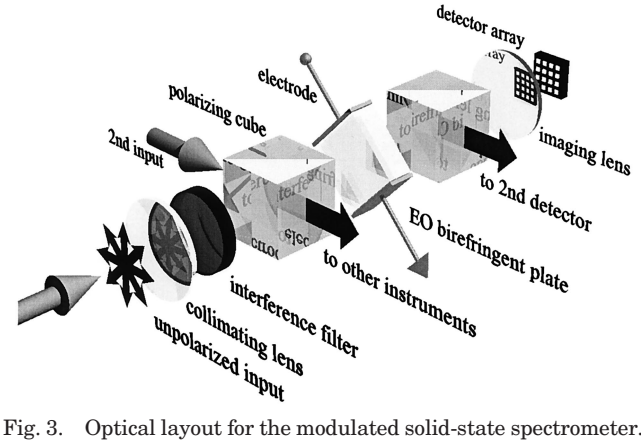


Fig. 3. Optical layout for the modulated solid-state spectrometer. EO, electro-optic.

(Pockels) effect. Writing $k_0 = 2\pi\nu_0/c$, a plate of thickness $L$ introduces a phase delay between the orthogonally polarized ordinary and extraordinary characteristic waves:

$$\phi_0 = k_0 BL = 2\pi\nu_0\tau_0 \equiv 2\pi N, \tag{15}$$

where $N$ is the order of interference. The delay modulation $\tilde{\phi}_1 = \phi_1 \sin \Omega t$ can be imposed when we apply an oscillating electric field along the crystal $Z$ axis transverse to the direction of the light propagation. The phase difference resulting from the applied field $V/d$, where $V$ is the potential difference and $d$ is the crystal width, is given by[9]

$$\phi_1 = \frac{\pi L V \delta}{\lambda_0 d}, \tag{16}$$

where $\delta = n_E{}^3 r_{33} - n_O{}^3 r_{13} = 2.325 \times 10^{-10}$ m/V is determined by the electro-optic tensor coefficients $r_{33} = 28.8 \times 10^{-12}$ m/V and $r_{13} = 7.7 \times 10^{-12}$ m/V. The modulation frequency can be freely chosen, although a driven response at frequencies well above or below the crystal acoustic resonant frequencies (in our case, ~120 kHz) is more likely to ensure a spatially uniform phase delay. Following the modulator, the light traverses a final polarizing cube to allow interference at detectors intercepting the transmitted and reflected beams.

Note that interference filters can be inserted at the separate output ports of the final polarizing cube, thereby allowing independent spectral lines to be measured simultaneously. For greater wavelength flexibility and improved background light rejection, the instrument can also be mounted at the input or output of a high-throughput, low-resolution grating spectrometer. The useful optical bandwidth is set by the properties of the $LiNbO_3$ plate, which is transparent in the range 0.4–5 μm. Use of β-barium borate crystals could allow operation well into the ultraviolet (>190 nm).

### C. Instrument Control, Data Acquisition, and Signal Processing

For the experiments reported here, the modulation frequency is typically $f = 40$ kHz. The high-voltage modulation of the electro-optic plate(s) is achieved with a function generator, a standard audio amplifier, and step-up transformer (100:1) to produce drive voltages of up to 4 kV p.p. at frequencies in the range 1–100 kHz. The transformer secondary output is connected across solid electrodes that cover the $Z$ surfaces of the electro-optic plate. When higher drive voltages are required, two transformers with their primaries in parallel (or separately driven by left and right audio-amplifier channels) and secondaries in series can be used to give double the drive voltage.

The light signals are low-pass filtered and amplified prior to data acquisition by use of $4f$, $8f$, or $16f$ synchronous external clocks, depending on the spread of harmonic carriers. The demodulation al-

gorithms (see Appendix A) self-consistently determine the drive modulation depth $\phi_1$ based on the relative amplitudes of the harmonic carriers. The spectral information is then extracted with a fast-Fourier-transform-based algorithm and returned with a bandwidth half of the separation of harmonic carriers (20 kHz).

For smaller modulation frequencies ($\lesssim$10 kHz), the low-level drive signal to the audio amplifier is provided by a PC card (PCI-MIO-16E-4) controlled with a LabVIEW virtual instrument (PCMOSS). The card software also acquires the MOSS signals and it processes, displays, and archives the data in real time.

## 4. Instrument Function

When using a grating spectrometer, it is important for one to know the overall broadband spectral response as well as more detailed information about the instrument dispersion, the slit function, and the absolute wavelength calibration. Here I evaluate the dual time-domain properties for the MOSS spectrometer, namely, the delay dispersion, instrument contrast (slit function), and absolute delay (wavelength calibration). I also compare the light throughput, or etendue, for the MOSS and grating spectrometers for high-resolution spectroscopic studies and consider the sensitivity of the width and shift estimates to light intensity noise.

### A. Spectral Response

Under white-light illumination, the MOSS spectral response shown in Fig. 4 was measured with a high-resolution grating spectrometer equipped with an image plane linear CCD detector array. Superimposed is the measured plasma spectrum in the vicinity of the 488-nm ArII emission line. The interferogram period, which is a rough measure of the interferometer spectral resolution $\nu_0/\Delta\nu = \nu_0\tau_0 = N$, is proportional to the birefringent phase delay (Subsection 4.B) and is chosen to be comparable with the spectral width of the emission line of interest. The fringe depth (visibility) is governed by the MOSS instrument contrast (Subsection 4.C) and the spectral width of the radiation (in this case, the grating spectrometer resolution). The apodizing envelope is a result of the interference filter that is used to reject light outside the passband of interest. Modulating the birefringent delay periodically shifts the interference pattern and allows discrimination of intensity variations that are due to changes in the center frequency or spectral width of the illumination.

### B. Delay Dispersion

As reflected in Eqs. (4) and (5), the interferometer phase delay at fixed frequency $\nu$ is given by $\phi = 2\pi LB(\nu)\nu/c = \phi_0 + \phi_0\xi$ where $\xi$ is the normalized frequency coordinate, $\phi_0 = 2\pi LB(\nu_0)\nu_0/c$ is the phase delay at the spectral line-center frequency $\nu_0$, $B(\nu)$ is the $LiNbO_3$ crystal birefringence, and $L$ denotes the crystal thickness. Because the interferometer integrates over all frequency components [see Eq. (5)], it

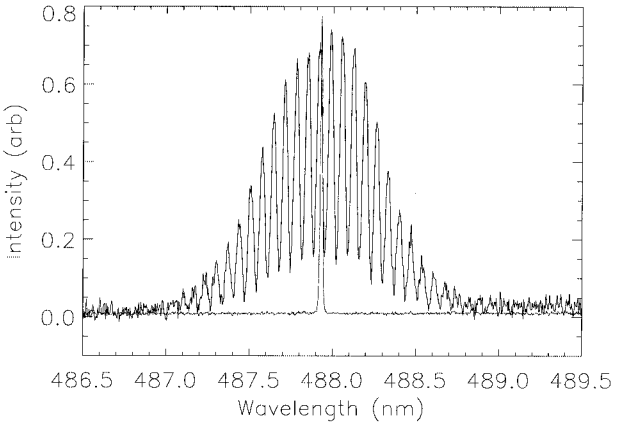


Fig. 4. Overlay of plasma spectrum in the vicinity of the 488-nm ArII line and the MOSS spectral response function. The interferogram is apodized by the narrow-bandpass interference filter that is used to isolate the spectral line from the plasma background. The period of the interferogram is inversely proportional to the MOSS interferometer delay (in this case, the crystal thickness is 24 mm) and is chosen to be comparable with the Doppler-broadened width of the emission line.

is necessary to take account of the birefringence dispersion when we evaluate the effective instrument delay. The birefringent phase delay at frequency $\nu = \nu_0 + \delta\nu$, where $\delta\nu$ is a small optical frequency shift, is given approximately by

$$\phi(\xi) = \phi_0 + \kappa\phi_0\xi, \tag{17}$$

where

$$\kappa = 1 + \frac{\nu_0}{B_0}\frac{\partial B}{\partial \nu} \tag{18}$$

accounts for the optical frequency dependence of the birefringence. The latter can be approximated by use of the Sellmeier equations for $n_E$ and $n_O$ (Ref. 8):

$$\begin{aligned} n_E^2(\lambda) &= 4.5820 + 0.099169/(\lambda^2 - 0.04443) \\ &\quad - 0.021950\lambda^2, \\ n_O^2(\lambda) &= 4.9048 + 0.11768/(\lambda^2 - 0.04750) \\ &\quad - 0.027169\lambda^2, \end{aligned} \tag{19}$$

where the wavelength $\lambda$ is in micrometers. Perhaps surprisingly, the correction term is of order unity, so that, for example, at 488 nm, $\kappa = 1.54$. Thus, for studies of the coherence of isolated spectral lines or multiplets, the crystal delay must be effectively scaled by the factor $\kappa$.

Figure 5 shows the wavelength dependence of the birefringence $B = n_E - n_O$ and the effective birefringence $\kappa B$ that follows from the frequency dispersion of $B$ in Eq. (5). Superimposed are experimental estimates of the effective delay obtained with measurement of the spectral response (as for Fig. 4 but with the interference filter removed) at a number of points in the visible spectrum.

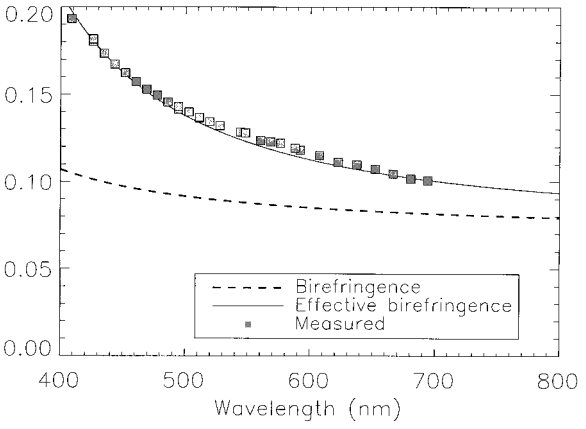


Fig. 5. Plot of the wavelength dependence of the birefringence for $LiNbO_3$ obtained by the Sellmeier equations. The dashed curve is the monochromatic birefringence, and the solid curve shows the calculated effective birefringence brought about by inclusion of the refractive-index dispersion. The filled squares are measurements obtained as discussed in the text.

### C. Instrument Contrast

For simplicity, let us ignore the spatial integration and assume a medium in drifting local thermodynamic equilibrium. Equation (14) becomes

$$S_{\pm} = I_0 \pm I_0\zeta \cos[\phi_0(1 + \kappa v_D) + \phi_1 \sin(\Omega t)], \quad (20)$$

where $\phi_0 + \delta\phi = \phi_0(1 + \kappa v_D)$ and $v_D$ is the component of the normalized flow velocity in the direction of view. The total fringe visibility $|\gamma| \equiv \zeta = \zeta_I\zeta_S$ includes an instrumental component $\zeta_I$ analogous to the familiar slit function for grating spectrometers, and $\zeta_S \equiv \exp(-T_S/T_C)$ is the contrast decrement that is due to the source temperature. The instrumental fringe contrast $\zeta_I$ is determined by the collected light solid angle and optical imperfections and can be represented by the constant factor $\zeta_I = \exp(-T_I/T_C)$, where $T_I$ is the instrument temperature. For the MOSS birefringent interferometer, we must modify the characteristic velocity to account for the birefringence dispersion by replacing $\phi$ with an effective delay $\phi_{\text{eff}} = \kappa\phi$ in Eq. (10). Because the interferogram is monitored at a single fixed delay, the source temperature $T_S$ can be obtained from the measured fringe contrast by a simple subtraction of exponents proportional to the measured and instrumental temperatures. This is in contrast with grating spectrometers that require noise-prone deconvolution of the instrument profile. At $T_S = T_C$ the interference contrast is reduced to $1/e$ of its maximum value. With this condition as a measure of the instrument resolving power $R_C$, Eq. (9) yields (see also Ref. 10)

$$R_C \equiv \frac{\nu_0}{\Delta\nu} = \pi N_{\text{eff}}, \quad (21)$$

where $N_{\text{eff}} = \phi_{\text{eff}}/2\pi = \kappa\phi/2\pi$.

The instrument fringe visibility (or temperature) is fundamentally limited by the range of angles subtended by the source, or the field of view. For small incidence angles $\theta_i$, the net delay between the characteristic $E$ and $O$ waves on propagation through the birefringent crystal is given by[11]

$$\phi \approx \phi_0\left[1 - \frac{\theta_i^2}{2n_O}\left(\frac{\cos^2\psi}{n_O} - \frac{\sin^2\psi}{n_E}\right)\right], \quad (22)$$

where $\psi$ is the azimuthal angle from the optic axis. We obtain the mutual coherence of the interfering waves at the detector by integrating over the source irradiance distribution (van Cittert–Zernike theorem). For a uniform, monochromatic circular source of solid angle $\Omega = \pi\theta_{\text{max}}^2$, the resulting instrumental coherence is given by

$$\gamma_I = \left(1 - \frac{\Omega^2N^2}{12n^4} + \ldots\right)\exp\left[-i\phi_0\left(1 - \frac{B\Omega}{8\pi n^3} + \ldots\right)\right], \quad (23)$$

so that

$$T_I \approx T_C\left(\frac{\Omega^2N^2}{12n^4}\right), \quad (24)$$

where $n$ is the mean refractive index. The visibility decrement that is due to the integration over a solid angle is negligible provided that the parameter $\epsilon = \Omega N/n^2$ is small. This condition shows the usual trade-off between resolving power $R_C \sim N$ and the collection solid angle, but is mitigated by a gain factor of $n^2/\sqrt{2}$ compared with a free-space Michelson interferometer. Further gain (field widening) can be achieved by use of crossed birefringent crystals with an intervening half-wave plate at an azimuth of 45°.[11,12]

For the experiments reported here (Section 6), we typically use a $LiNbO_3$ plate of thickness 25 mm, yielding an effective optical delay $N_{\text{eff}} \sim 8000$ waves and a nominal wavelength resolution of 0.02 nm at 488 nm. Light is generally relayed to the instrument by use of optical fibers of diameter 1 mm and numerical aperture N.A. $\simeq 0.3$ coupled to the MOSS spectrometer with an $F/1.4$ collimating lens of focal length 50 mm. The resulting collimated beam half-angle $\theta_{\text{max}} \sim 0.006$ combined with absolute delay $N_{\text{eff}} \sim 8000$ yields $\epsilon \sim 0.1$ so that the decrement in fringe contrast that is due to the field of view is small. Depending on the quality of the birefringent plate(s), the measured instrumental fringe visibility is generally in the range $\zeta_I = \exp(-T_I/T_C) \sim$70–90% at 488 nm corresponding to $T_I/T_C \sim 0.35$–0.1.

Reasons for less than ideal fringe visibility can include unequal surface reflection losses for polarization components parallel and perpendicular to the optic axis, crystal birefringence inhomogeneities, surface nonparallelism or optic axis misalignment, nonunity extinction ratio for the polarizing cubes, and misalignment of the optical components. Imperfect polarizing cube extinction is important for the reflected wave, which can contain nonnegligible contamination from the $P$-polarization component. The

maximum fringe visibility in this case is $\zeta_P = (1 - \rho)/(1 + \rho)$ where $\rho$ is the ratio of the power reflectivities for the $P$ and $S$ components. For small $\rho$ (broadband polarizing cubes typically have $\rho \lesssim 0.08$ at 488 nm) we obtain an equivalent instrument temperature $T_I \approx 2\rho T_C$. This significant contrast degradation is removed by means of an additional polarizing optic at the reflection port.

Other effects that can compromise the instrument contrast include the combined action of piezoelectric and acousto-optic effects at high electric field strengths. These distortions, which are important for modulation frequencies less than the crystal acoustic resonances, result in a variation of the instrument fringe contrast at the modulation frequency with a resulting $\phi_0$-dependent effective decrease of the instrument contrast. However, for typical drive voltages used in our experiments, measurements of the instrument fringe contrast variation with $\phi_0$ show this to be a small effect (standard deviation of 1% of the mean $\zeta_I$).

### D. Instrument Delay

Because of uncertainties in the absolute determination of the crystal delay $\phi_0$ that are due, for example, to thermal drifts of the refractive index, calibration of the interferogram phase for absolute flow velocity measurements requires comparison with light emitted from a standard source, preferably from an identical emission line generated by a spectral calibration lamp or laser. The appearance of the instrumental phase $\phi_I$ also requires that light from both plasma and calibration sources be injected with a common geometry so that this phase offset is compensated. This can be arranged, for example, by use of lens-coupled optical fibers to relay light from either source to the spectrometer. For the study of quasi-continuous plasmas, it may be possible to actively compensate slow thermal drifts in $\phi_{\text{eff}}$ with an independent calibration source (spatially or temporally multiplexed) to control an adjustable dc bias voltage applied to the electro-optic crystal. In the absence of a suitable calibration source, or careful temperature stabilization, only relatively fast temporal changes in the mean normalized flow speed $\delta v_D$ can be accurately measured. The absolute value of these changes is easily calculated from the measured phase shift and the estimated initial dc phase offset $\phi_0$.

### E. Light Throughput

It is instructive to compare the light thoughput for the MOSS spectrometer and a grating spectrometer of equivalent resolving power. A standard $F/5$ grating spectrometer of focal length 0.5 m equipped with a 2400-lines/mm grating operating in first order and with a 25-$\mu$m slit width will yield $R \sim 5000$. Taking the slit height to be equal to the 20-mm clear diameter of the interference filter—the primary limiting aperture for the MOSS spectrometer—the grating spectrometer etendue is $E_G = A_G\Omega_G = 0.008$ sr/mm$^2$, where $A_G = 25\ \mu\text{m} \times 20$ mm is the slit area and $\Omega_G$ is the collection solid angle set by the spectrometer $F$-number. We obtain the limiting field of view for the MOSS spectrometer by setting $T_S = T_C$ in approximation (24) to obtain for the MOSS etendue $E_M = 0.9$ sr/mm$^2 \sim 120E_G$. With field widening, or larger apertures, the etendue disparity can be even greater, although ultimately the amount of light collected from the source may be limited by spatial resolution considerations rather than the etendue of the dispersing instrument.

### F. Noise Sensitivity

The instrument temperature plays an important role in the determination of the sensitivity of the MOSS signal to changes in spectral bandwidth (or source temperature in Doppler applications). Without regard to the details of the demodulation scheme, a rough estimate of the sensitivity of the signal [Eq. (20)] to temperature changes is given by

$$\alpha_T \equiv \max_{\phi}\left(\frac{\partial S}{\partial T_S}\right) = -\frac{I_0}{T_C}\,\zeta. \tag{25}$$

The sensitivity deteriorates when the instrument fringe contrast is poor and attains a maximum with respect to $T_C$ when $T_S + T_I = T_C$ (provided that $T_I < T_C$).

The ability to distinguish changes in light intensity arising from temperature variations is, at best, determined by the intensity Poisson noise. The signal sensitivity to this noise, averaged over a modulation period, is given by $\bar{\alpha}_I \equiv \overline{(\partial S/\partial I_0)} = 1$. The sensitivity of the inferred temperature to photon shot noise is estimated when we set $\mathrm{d}S = \bar{\alpha}_I \mathrm{d}I_0 + \alpha_T \mathrm{d}T_S = 0$ to obtain

$$\frac{\mathrm{d}I_0}{I_0} = \zeta\frac{\mathrm{d}T_S}{T_C}. \tag{26}$$

This shows that, for a given light noise level, the absolute uncertainty in the inferred temperature increases as fringe visibility decreases. Equation (26) can also be written as

$$\frac{\mathrm{d}T_S}{T_S} = k_T(r)\,\frac{\mathrm{d}I_0}{I_0}, \tag{27}$$

where $r = T_S/T_C$ and $k_T(r) = \exp r/r$ is the factor relating the fractional light noise level with the relative uncertainty in the inferred species temperature. The behavior of $k_T(r)$ as a function of normalized species temperature $r$ is shown in Fig. 6. The MOSS spectrometer is most sensitive to relative changes in $T_S$ when $T_S = T_C$. For the H-1 system, and at $T_S = T_C = 36$ eV, intensity noise of the order of 5% corresponds to temperature uncertainties of approximately 4 eV. The divergence at small $r$ is due to the nature of the exponential relationship between measured contrast and source temperature. We can increase the dynamic range effectively by cascading instruments having different delays (see below) or by using multiple birefringent plates mutually aligned at 45°.

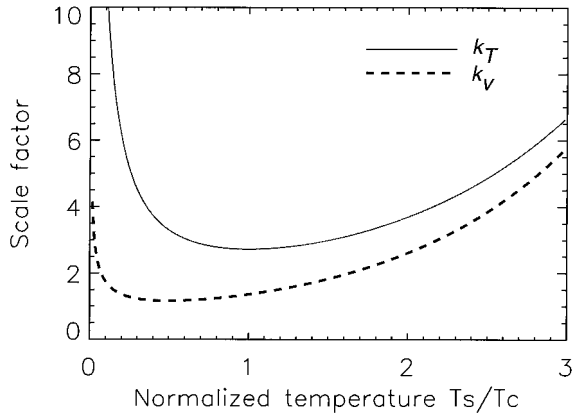


Fig. 6. Dependence of the scaling functions $k_T(r)$ and $k_v(r)$ relating the fractional light noise and the relative uncertainty in the inferred temperature $T_S$ and drift velocity $v_D$ as a function of the normalized temperature $r = T_S/T_C$.

A higher source temperature requires a higher value of $T_C$ for an optimum signal-to-noise ratio. Combining Eqs. (9) and (15) shows that $T_C$ is proportional to $1/L^2$ so that the voltage required to obtain at least a $\pi/2$ modulation depth is proportional to $T_C{}^{1/2}$. We can overcome this practical difficulty by reducing the crystal aperture, but with some attendant loss of light throughput. An alternative approach is to combine crystals so that their individual delays subtract while the modulation voltages are of opposite polarity. In this case, however, the instrument temperature is also increased unless a half-wave matching plate (field widening) is used.

The sensitivity to flow speed changes is estimated by

$$\alpha_v \equiv \max_{\phi}\left(\frac{\partial S}{\partial v_D}\right) = I_0\zeta\kappa\phi. \tag{28}$$

With respect to the characteristic temperature $T_C$, the maximum sensitivity to flow speed variations occurs when $T_S + T_I = T_C/2$. This optimum value is obtained because the increase in sensitivity to $v_D$ with delay $\phi$ is counteracted by a decrease in contrast $\zeta$.

When the temperature is constant, the ability to resolve small flow velocity changes depends on the light signal-to-noise ratio. Setting $dS = \bar{\alpha}_I dI_0 + \alpha_v dv_D = 0$, we obtain

$$\frac{dv_D}{v_{th}} = k_v(r)\,\frac{dI_0}{I_0}. \tag{29}$$

$v_{th} = (2kT_S/m_S)^{1/2}$, and the scaling factor $k_v = \exp(r)/2\sqrt{r}$ analogous to $k_T$ is also shown in Fig. 6. For argon at $T_S = T_C/2 = 18$ eV, $v_{th} \approx 9 \times 10^3$ m/s, implying a velocity resolution $\delta v_D \sim 600$ m/s for $\delta I_0/I_0 = 0.05$. Simulations confirming the form of the noise sensitivity factors displayed in Fig. 6 also indicate a slow dependence on modulation depth $\phi_1 \gtrsim \pi/2$ that is optimum for $\phi_1 \sim 130°$ (see also Ref. 13).

## 5. Test Results

### A. Contrast Measurements with a Magnetized Lamp

To test the MOSS performance, and to confirm the effects of delay dispersion, my colleagues and I used the instrument to measure the Zeeman splitting of the $^3S_1$–$^3P_0$ transition at 468 nm ($\kappa = 1.60$) in a zinc dc discharge lamp (18 V, 2 A) placed between the poles of a Helmholtz coil electromagnet. Observing in a direction perpendicular to the magnetic field, the first MOSS polarizer was oriented so as to transmit only the two outer $\sigma$ components ($\Delta M = \pm 1$ where $M$ is the magnetic quantum number) of the normal triplet. The MOSS then detects the superposition of the separate interferograms:

$$S = \frac{I_0}{8}\,[1 + \zeta\,\cos(2\pi\nu_+\tau_+)] + \frac{I_0}{8}\,[1 + \zeta\,\cos(\pi\nu_-\tau_-)]$$

$$= \frac{I_0}{4}\,[1 + \zeta\,\cos(\kappa\phi_0\xi_B)\cos\,\phi_0], \tag{30}$$

where $\zeta$ is the fringe contrast, $I_0$ is the brightness of the full triplet, and $\tau_\pm$ are the birefringent delays at optical frequencies $\nu_\pm = \nu_0 \pm \Delta\nu_B$. The beating of the two interferograms gives rise to a $B$-dependent cosinusoidal modulation of the fringe contrast $\cos(\kappa\phi_0\xi_B)$ where $\xi_B = \Delta\nu_B/\nu_0$ is the normalized Zeeman frequency shift with

$$\Delta\nu_B = \frac{geB}{4\pi m_e} \tag{31}$$

and $g = 2$ is the Landé splitting factor. We can measure the fringe contrast by electro-optically modulating the phase delay as explained above.

With the PCMOSS system used for data acquisition, the magnetic field was ramped and the demodulated MOSS interferogram was recorded. The magnetic field strength is monitored by a Hall probe whose calibration was checked against standard magnets and confirmed by measurements of the Zeeman splitting by use of a high-resolution grating spectrometer. Figure 7 shows the recorded fringe contrast modulation versus the magnetic field strength obtained by a four-crystal MOSS system of total thickness $L = 100$ mm. Superimposed is the expected contrast modulation. The close agreement confirms the result for the wavelength-dependent delay dispersion given by Eq. (17).

### B. Intensity and Phase Measurements with a Modulated Laser

Calibration tests were performed on a single MOSS spectrometer with a 25-mm-thick $LiNbO_3$ plate and with an expanded He–Ne laser (632.8 nm) as a light source. The laser beam was chopped to allow for subtraction of the signal baseline. To check the linearity and integrity of the hardware and software systems, a low-frequency (50-Hz) triangle wave of adjustable amplitude was superimposed on the sine-wave modulator signal ($\Omega/2\pi = 6$ kHz) prior to am-

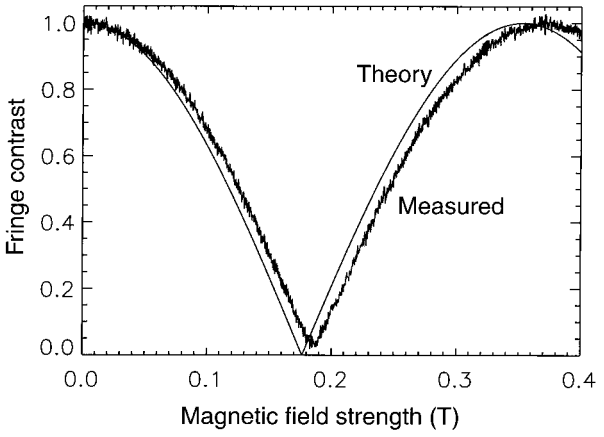


Fig. 7. Measured interferogram contrast modulation for the two σ components of the Zeeman split triplet versus magnetic field strength. The beat period of the respective interferograms is a measure of the MOSS delay dispersion. The theoretical curve based on the calculated delay dispersion ($\kappa = 1.6$) for $LiNbO_3$ crystals is a reasonable match to the measurements.

plification to high voltage. This modulates the phase offset $\phi_0$ to simulate a spectral line whose center frequency varies in a similar triangle fashion. The composite high-voltage signal applied across the $LiNbO_3$ plate is shown in Fig. 8(a). In addition to the phase modulation, the laser intensity was also amplitude modulated at 600 Hz with electro-optic techniques. The interferogram at the transmit port of the final polarizer is shown in Fig. 8(b). The demodulated light intensity, instrumental fringe contrast, and phase $\phi_0$ are shown in Figs. 8(c)–8(e). The dashed curves are the demodulated quantities obtained from light at the final polarizer reflection port. The imposed modulations are retrieved with a low level of cross talk. Note also the consistency of the inferred contrast and phase for reflected and transmitted signals. The expected phase excursion of 190° at 632.8 nm for an applied sawtooth of amplitude 3.2 kV agrees reasonably well with the measured amplitude ~175°.

### 6. Plasma Doppler Measurements

The H-1 heliac is a helical-axis toroidal magnetic plasma confinement device having major radius $R = 1$ m and a beam-shaped plasma cross section of average minor radius $a \sim 0.2$ m.[3] The high light throughput afforded by MOSS allows detailed studies of the temporal evolution of line-integrated ion flow speeds and temperatures. Such measurements allow us to estimate the internal plasma electric field by studying the balance between electromagnetic and pressure forces. I show results for rf-generated (7-MHz, 60-kW, ~100-ms) discharges in argon at low magnetic field strength ($\lesssim 0.2$ T). In this regime, the plasma undergoes spontaneous transitions between low and high particle and energy confinement. These transitions have been shown to be related to changes in the radial plasma electric potential profile with an associated influence on the nature of plasma

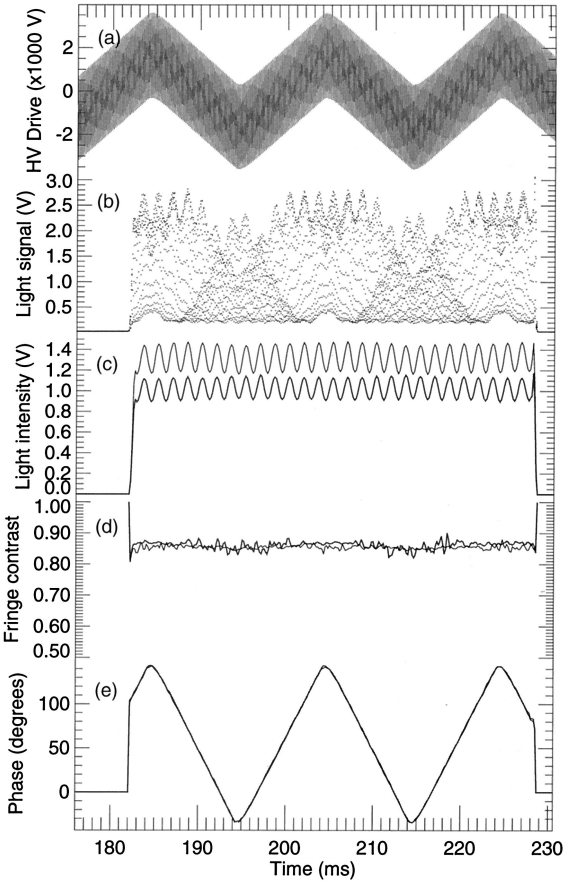


Fig. 8. Plot showing the MOSS calibration data obtained at 632.8 nm. (a) The high-voltage (HV) signal (triangle-wave plus sine-wave modulation) applied to the $LiNbO_3$ plate. (b) The modulated signal at the polarizer transmit port. Demodulated quantities (solid curves, transmit port; dashed curves, reflect port): (c) laser light intensity, (d) instrument contrast, (e) phase offset.

instabilities that can degrade the machine performance.[14]

Figure 9 shows a dual MOSS system that combines separate spectrometers having crystal thicknesses of 25 and 40 mm ($T_C = 36$ eV and $T_C = 14$ eV, respectively, at 488 nm). The MOSS optical components are mounted inside a light-tight housing, and photo-

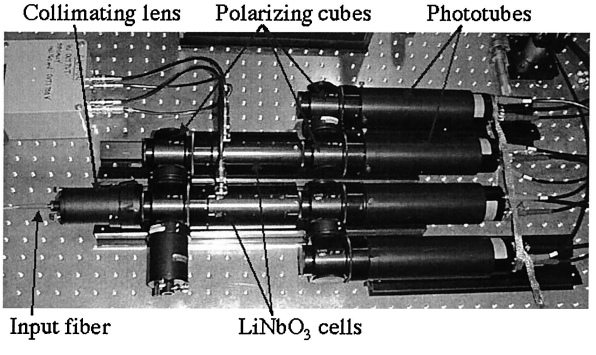


Fig. 9. Photograph of the dual MOSS spectrometer with major components labeled.

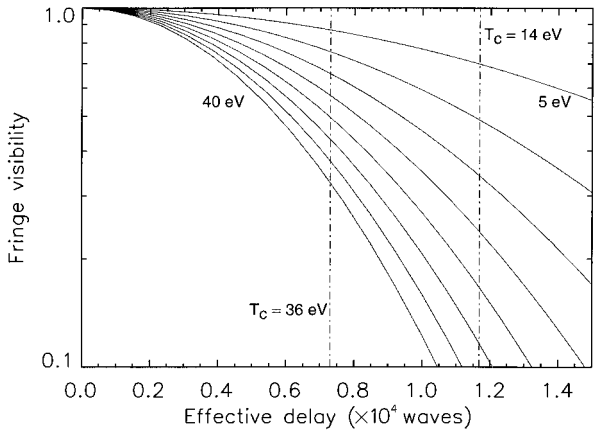


Fig. 10. Plot of fringe contrast versus FTS phase delay for a uniform plasma with ion temperatures 5, 10, 15, . . . , 40 eV. The vertical lines correspond to the delays introduced by 25- and 40-mm $LiNbO_3$ cells at 488 nm. Note particularly the wide dynamic range for sensitivity to temperature changes.

multipliers are used for detection. The 40-mm delay is obtained when separate plates of thicknesses 15 and 25 mm are combined. Observed ion temperatures in the range 5–25 eV match well the dynamic range spanned by the dual MOSS system, as can be seen in Fig. 10, which shows the variation of fringe contrast $\zeta_S$ with delay $\phi_{\text{eff}}$ for argon-ion temperatures in this range. The vertical lines correspond to the delays introduced by the 25 and 40-mm-thick $LiNbO_3$ crystals at 488 nm. Observe that, for a given delay, a 90% variation in fringe contrast represents roughly an order-of-magnitude variation in temperature. The net delay can be tailored according to Eq. (21) to obtain an instrument resolution appropriate for the expected spectral linewidth.

The instrument contrast, measured with an expanded argon-ion laser beam at 488 nm, is typically 0.7 and arises mainly from imperfections in the birefringent plate. Light from a beam-expanded argon-ion laser, suitably attenuated to match the plasma light intensity and temporally gated so as not to coincide with the plasma pulse, can be admitted through the unused input port of the first polarizing cube. As well as being used to estimate the instrument contrast, this light signal can be used to compare the level of photon shot noise with the natural plasma light fluctuation level.

A number of light collection systems have been installed on the H-1 heliac. These include fixed intravacuum lens-coupled optical fibers to monitor emission integrated in the toroidal (horizontal) direction and externally mounted lens-coupled fibers that can be translated across the poloidal (vertical) cross section on a shot-to-shot basis as can be seen in Fig. 11.

Figure 12 shows data for a low field (~0.14 T) discharge that dithers between states of low and high confinement. The electron density is measured with a swept-frequency millimeter-wave interferometer. The interferometer beam probes along the plasma along the plasma minor radius in a poloidal cross

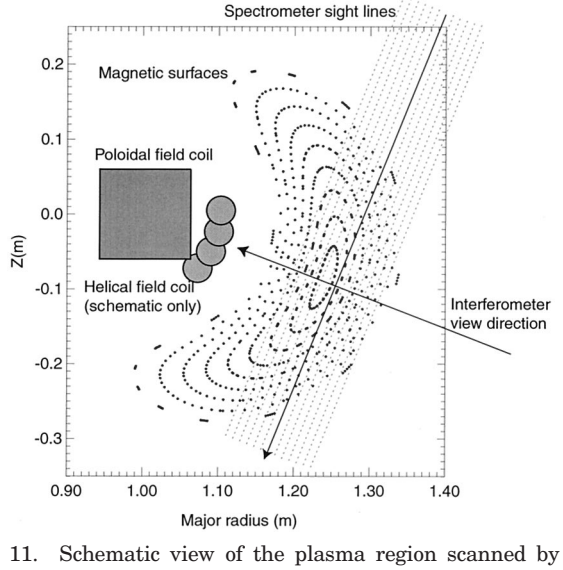


Fig. 11. Schematic view of the plasma region scanned by the solid-state spectrometer.

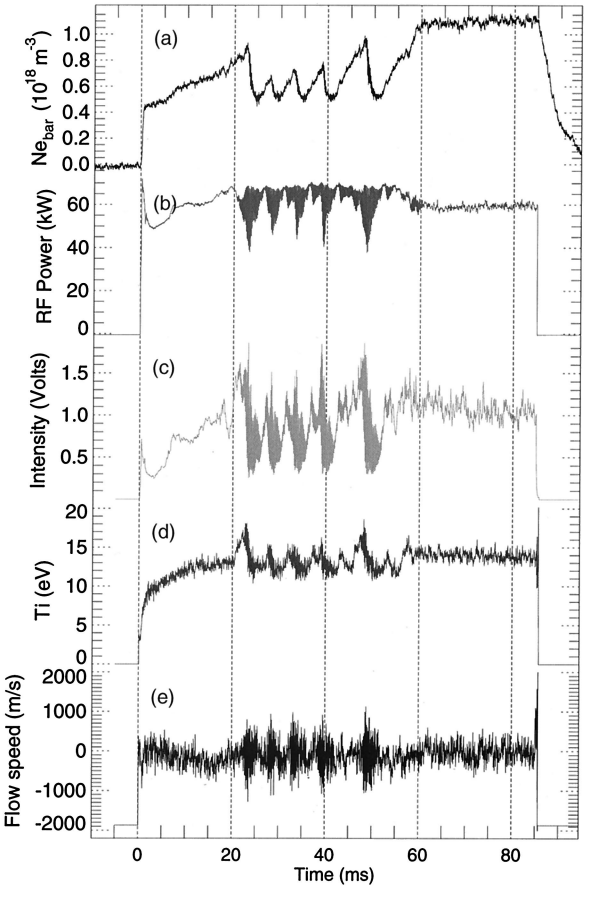


Fig. 12. Plot showing plasma parameters for a discharge that dithers between regimes of poor and high confinement. (a) The line-of-sight averaged electron number density, (b) the absorbed rf power, (c) the plasma light intensity, (d) ion temperature, (e) toroidal flow velocity.

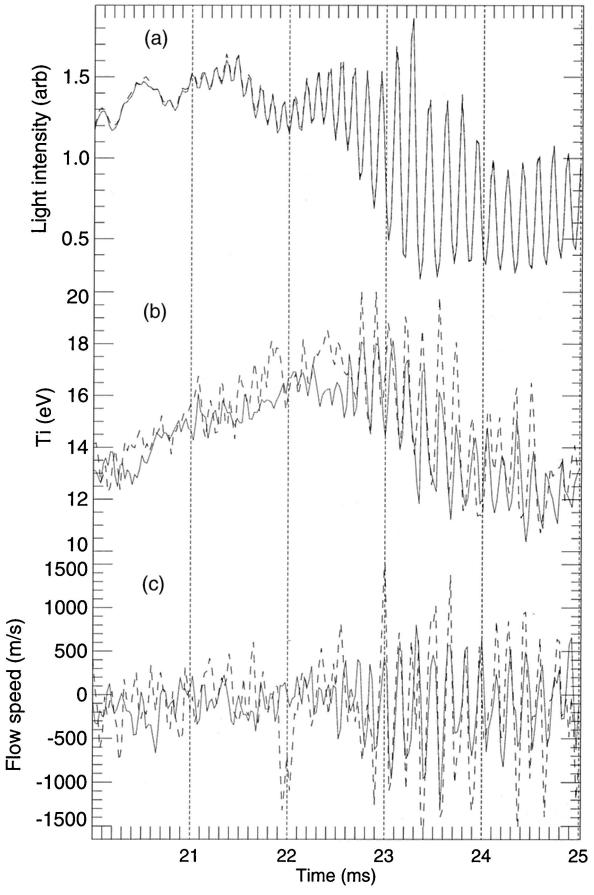


Fig. 13. Plot showing detailed comparison of data extracted from the dual MOSS system. Solid curves, $T_C$ = 14-eV cell; dashed curves, $T_C$ = 36-eV cell. (a) The extracted light intensities, (b) ion temperatures, (c) toroidal flow speeds.

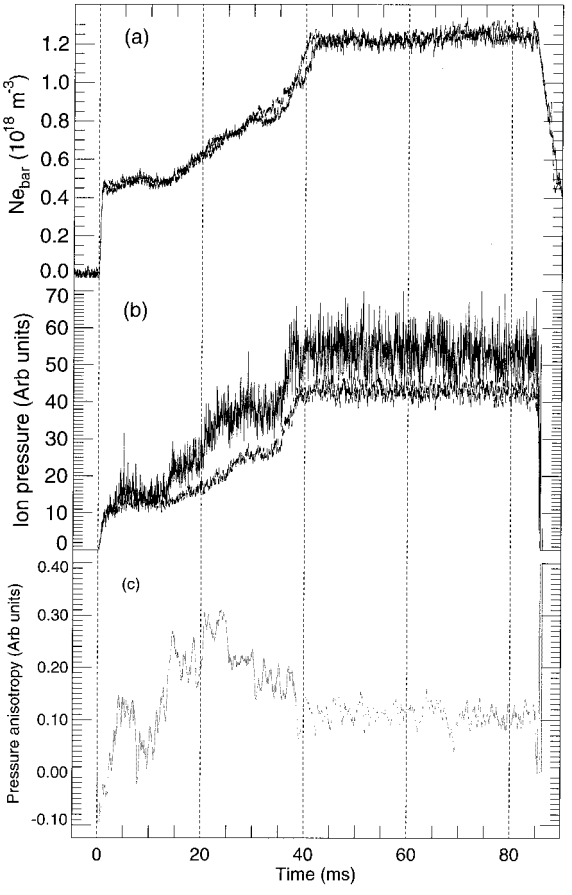


Fig. 14. Comparison of perpendicular and parallel ion pressure for nominally identical discharges. (a) Superposition of electron density traces (solid curve, parallel; dashed curve, perpendicular), (b) ion pressure, (c) pressure anisotropy. See text for discussion.

section as shown in Fig. 11. Also shown is the rf power delivered to the plasma and the light intensity, ion temperature, and the flow speed inferred from the MOSS interferogram. The light was collected from an approximately cylindrical plasma volume of diameter 30 mm with an axis tangent to the plasma magnetic axis that points in a predominantly toroidal direction (normal to the page in Fig. 11). The displayed data were obtained by use of the 40-mm crystal cell with characteristic temperature $T_C$ = 14 eV at 488 nm. The intensity-weighted temperature is obtained from the logarithm of the fringe visibility [Eq. (11)], and the flow is estimated directly from the measured phase shift by use of Eq. (20).

It is apparent from the light intensity that, as the central plasma density increases (increased density gradient), a strong coherent instability is excited that spoils the plasma confinement, leading to a collapse in the internal plasma ion pressure ($nT_i$). The instability has an odd parity angular structure and so couples only weakly to the interferometer signal. Coherent perturbations to the ion temperature and toroidal flow speed also attend the onset of instability. The high light throughput and time-domain modulation techniques employed by MOSS allow these oscillations to be resolved.

The consistency of the extracted plasma-related quantities from both 25- and 40-mm cells is illustrated in Fig. 13, which shows data for the time interval around the first confinement collapse. Data for the 25-mm cell ($T_C$ = 36 eV) are plotted as the dashed curves. Given that the received intensities are comparable, the lower noise for data from the 40-mm cell (solid curves) is due to the fact that the ion temperature more closely matches $T_C$ = 14 eV. The inferred flows were both adjusted to be zero at the commencement of the plasma pulse. In general, good global and detailed agreement is found between these independent estimates of the plasma dynamical quantities. That the flow velocities obtained at the different delays agree within experimental uncertainty is consistent with the assumption of a locally drifting distribution.

The temporal evolution of ion temperature measurements made in a toroidal direction (tangential to the magnetic axis) and along a central poloidal chord transverse to the magnetic axis (see Fig. 11) are compared in Fig. 14. These nominally identical dis-

charges obtained at the slightly increased field strength ~0.16 T now exhibit an uninterrupted transition from low to high confinement (the net rf absorbed power stays relatively constant at 60 kW). A strong persistent ion temperature anisotropy, together with a slightly hollow transverse temperature profile, suggests that ions can be heated in the sheath region of the rf antenna that resides close to and conforms with the outer half of the plasma poloidal cross section. The degree of anisotropy $(p_\perp - p_\parallel)/(p_\perp + p_\parallel)$ plotted in Fig. 14(c) is greatest during the approach to the transition at $t = 35$ ms and appears to be inversely related to the electron number density.

### Appendix A: Demodulation Algorithm

We assume that the sampling rate is sufficiently high to capture all significant harmonic information and that the data are suitably prefiltered to avoid the aliasing of broadband noise.

Using the Bessel function expansion for the trigonometric terms, we can express the Fourier transform of Eq. (14) as

$$S_\pm(f) = \mathcal{I}(f) \pm \sum_n J_{2n}(\phi_1)\mathcal{C}(f - 2nf_m) \pm i \sum_n J_{2n+1}(\phi_1)\mathcal{Q}[f - (2n+1)f_m], \quad \text{(A1)}$$

where $f_m = 1/T = 2\pi/\Omega$ is the modulation frequency and

$$\mathcal{I}(f) = \mathcal{F}(I_0), \quad \mathcal{C}(f) = \mathcal{F}(I_0\gamma_c), \quad \mathcal{Q}(f) = \mathcal{F}(I_0\gamma_q) \quad \text{(A2)}$$

are the Fourier transforms of the interferometric information. We assume that the information bandwidth required for these terms is less than $f_m/2$ (half of the separation of the carrier harmonics) and ignore noise components.

To recover the information, we apply bandpass filters of width $\Delta f = f_m$ centered at frequencies $nf_m$, translate to zero frequency, and perform the inverse Fourier transform. The signal spectrum occupying the $k$th frequency passband $(k - 1/2, k + 1/2)f_m$ is written as

$$S_\pm^{(k)}(f) \equiv \Pi\left(\frac{f}{f_m}\right) S_\pm(f + kf_m). \quad \text{(A3)}$$

Given the Hermitian symmetry $S_\pm^{(k)}(f) = S_\pm^{(k)*}(-f)$, it is sufficient to consider only positive harmonics $k$.

Taking the inverse Fourier transform of the spectral terms $S_\pm^{(k)}$ delivers temporal signals

$$S_\pm^{(2k+1)} = \pm I_0\gamma_q J_{2k+1}, \quad S_\pm^{(2k)} = \pm I_0\gamma_c J_{2k} \quad k > 0, \quad S_\pm^{(0)} = I_0 \pm I_0\gamma_c J_0. \quad \text{(A4)}$$

For modulation depth $\phi_1 \gtrsim \pi/2$, the signals associated with the three lowest-order harmonics are dominant and are sufficient to determine the unknown quantities $I_0$, $\gamma_q$, and $\gamma_c$. However, it is advantageous to sum like harmonic terms to obtain $S^{\text{odd}} = \sum_k^K S^{(2k+1)}$ and $S^{\text{even}} = \sum_k^K S^{(2k)}$ where the truncation at $k = K$ is determined by the level of noise compared with the Bessel-weighted information. A simple algorithm can be applied to yield noise-tainted estimates of the fringe visibility and phase:

$$\gamma \equiv |\gamma| = (Q^2 + C^2)^{1/2}/I_0, \quad \text{(A5)}$$

$$\phi = \arctan(Q/C), \quad \text{(A6)}$$

where

$$Q(t) = S^{\text{odd}}/\sum_k^K J_{2k+1}, \quad \text{(A7)}$$

$$C(t) = S^{\text{even}}/\sum_k^K J_{2k}, \quad \text{(A8)}$$

$$I_0(t) = S^{(0)} + J_0 C(t). \quad \text{(A9)}$$

I am grateful to Clive Michael for many useful discussions and thank A. Danielsson for help with the Zeeman effect calibration experiments.

### References


1. J. Howard, "Modulated Optical Solid-State spectrometer applications in plasma diagnostics," Rev. Sci. Instrum. **70,** 368–371 (1999).
2. J. Howard, "Optical coherence-based techniques for motional Stark effect measurements of magnetic field pitch angle," Plasma Phys. Controlled Fusion **41,** 271–284 (1999).
3. S. Hamberger, B. Blackwell, L. Sharp, and D. Shenton, "H-1 design and construction," Fusion Technol. **17,** 123–130 (1990).
4. J. Howard, "Vector tomography applications in plasma diagnostics," Plasma Phys. Controlled Fusion **38,** 489–503 (1996).
5. R. Hilliard and G. Shepherd, "Upper atmosphere temperatures from Doppler line width," Planet. Space Sci. **14,** 386–406 (1966).
6. G. Thuillier and M. Hersé, "Thermally stable field compensated Michelson interferometer for measurement of temperature and wind of the planetary atmospheres," Appl. Opt. **30,** 1210–1220 (1991).
7. W. Gault, S. Brown, A. Moise, D. Liang, G. Sellar, G. Shepherd, and J. Wimperis, "ERWIN: an E-region wind interferometer," Appl. Opt. **35,** 2913–2922 (1996).
8. R. S. Weiss and T. K. Gaylord, "Lithium niobate: summary of physical properties and crystal structure," Appl. Phys. A **37,** 191–203 (1985).
9. I. P. Kaminow, *An Introduction to Electrooptic Devices* (Academic, New York, 1974).
10. A. P. Thorne, *Spectrophysics* (Chapman & Hall, London, 1988).
11. W. Steel, *Interferometry* (Cambridge U. Press, Cambridge, UK, 1967).
12. C. Michael, J. Howard, and B. D. Blackwell, "The MOSS camera on H-1NF," Rev. Sci. Instrum. **72,** 1034–1037 (2001).
13. O. Sasaki and H. Okazaki, "Analysis of measurement accuracy in sinusoidal phase modulating interferometry," Appl. Opt. **25,** 3152–3158 (1986).
14. M. Shats, D. L. Rudakov, B. D. Blackwell, G. Borg, R. L. Dewar, J. Howard, and L. Sharp, "Improved particle confinement mode in low-temperature plasma in H-1 heliac," Phys. Rev. Lett. **77,** 4190–4193 (1996).